Journal of
Instrumentation

PAPER • OPEN ACCESS

In-situ calibration of charge exchange spectroscopy for spatially resolved measurements of helium-hydrogen density ratio in Wendelstein 7-X

To cite this article: M. Yoshinuma *et al* 2025 *JINST* **20** P07006

Published by IOP Publishing for Sissa Medialab

Received: *March 14, 2025*
Revised: *March 31, 2025*
Accepted: *June 12, 2025*
Published: *July 4, 2025*

In-situ calibration of charge exchange spectroscopy for spatially resolved measurements of helium-hydrogen density ratio in Wendelstein 7-X

M. Yoshinuma,[a] **K. Ida**,[a,*] **O.P. Ford**,[b] **P.Z. Poloskei**,[b] **T. Romba**,[b] **M. Zanini**,[b] **J. Baldzuhn**,[b] **K. Rahbarnia**,[b] **H. Thomsen**,[b] **U. Neuner**,[b] **M. Zilker**[b] **and W7-X Team**[b,1]

[a] *National Institute for Fusion Science, National Institutes of Natural Sciences, Toki, Gifu 509-5292, Japan*
[b] *Max-Planck Institut für Plasmaphysik, 17491 Greifswald, Germany*

E-mail: Ida.katsumi@nifs.ac.jp

Abstract: In-situ calibration of charge exchange spectroscopy for spatially resolved measurements of helium-hydrogen density ratio is described in this paper. The helium-hydrogen density ratio in the core plasma is derived from the intensity ratio of the active helium line HeII (468.6 nm) and hydrogen line HI (656.3 nm) due to the charge exchange recombination process between fully ionized ions and neutral beam. This system is calibrated by the helium-hydrogen density ratio evaluated from HeII (656.0 nm) and HI (656.3 nm) in the recombining phase at the end of the discharge. The helium-hydrogen density ratio at the plasma center derived from the calibrated charge exchange spectroscopy is compared with the influx ratio estimated from the passive spectroscopy.

Keywords: Plasma diagnostics - interferometry, spectroscopy and imaging; Nuclear instruments and methods for hot plasma diagnostics

*Corresponding author.
[1] For the complete member list, please refer to T. Sunn Pedersen, *Nucl. Fusion* **62** (2022) 042022.

https://doi.org/10.1088/1748-0221/20/07/P07006

Contents

1 Introduction

Measurements of hydrogen fraction in the core region of hydrogen and helium plasma are indispensable for ion cyclotron resonance heating (ICRH) in helium-hydrogen mixture plasmas because the heating efficiency strongly depends on the hydrogen fraction of $n_H/(n_H + n_{He})$. So far at Wendelstein 7-X, the intensity ratio of helium to hydrogen, I_{He}/I_H, measured with passive spectroscopy, is used as a reference of hydrogen fraction. However, passive spectroscopy gives information about the influx (particle source at the plasma edge) but not the density ratio in the core plasma. These will deviate significantly when core fuelling methods such as neutral beam or pellet injection are used and also if the location of the flux measurement is not representative of the average influx ratio across the large wall area. This motivates the need for density ratio measurement. Charge exchange spectroscopy is a powerful tool for measuring the ion density in the plasma for low-Z impurity (Beryllium, carbon, Oxygen) [1–5], helium [6–8], and bulk (hydrogen and deuterium) [9–11]. Recently, the isotope ratio between hydrogen an deuterium has also been measured with charge exchange spectroscopy. Although the charge exchange spectroscopy gives a radial ion density profile, absolute calibration is complex and will not be possible in future machines, e.g. reactors and ITER. In the conventional approach, the absolute density is derived from the absolute calibrated intensity of the charge exchange line, beam density by the beam attenuation code, and emission cross-section [2–5]. However, the absolute density has a significant error due to the uncertainty of the emission cross-section, which depends on the atomic model [12] and the fraction of electron in metastable state (excited $n = 2$ level) [5, 13, 14]. Once the radial profiles of the hydrogen/deuterium isotope ratio are measured, the absolute density of hydrogen and helium can be readily evaluated from the electron density profiles using a quai-neutralization condition in most discharges where the other impurity concentration is reasonably low.

An in-situ calibration technique for charge exchange spectroscopy has been proposed in LHD to improve the accuracy of the impurity density measurements. One technique is in-situ calibration using the impurity pellet, while the other uses the recombining phase at the end of the discharge. Because both the charge exchange line intensity and electron density significantly increase after the impurity pellet injection, the impurity density can be calibrated by the increment of electron density measured with YAG Thomson scattering [15]. This is an excellent approach to in-situ calibration for impurities where a solid impurity pellet can be injected but is ineffective for measuring helium impurities because

2025 JINST 20 P07006

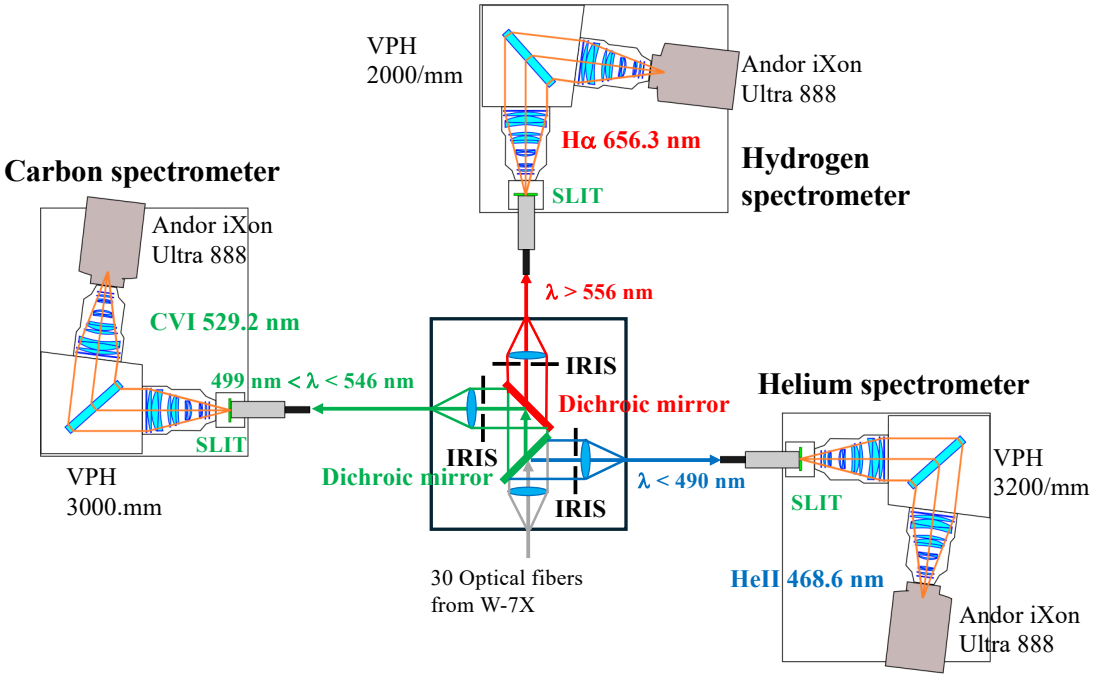

Figure 1. Diagram of the setup of charge exchange spectroscopy for helium, hydrogen, and carbon.

the number of ions supplied to the plasma by gas puff is unknown. The in-situ calibration using the recombining phase is very effective for measuring helium-to-hydrogen density ratio profiles [7]. Because the helium-to-hydrogen ratio profile has a variety (peaked, flat, or hollow) depending on the discharge condition [8], the calibrated charge exchange spectroscopy is indispensable to derive the helium-to-hydrogen density ratio at the plasma center. This paper describes the in-situ calibration of NIFS charge exchange spectrometers installed on Wendelstein 7-X [16]. The comparison between the core density ratio and the influx ratio estimated from the passive spectroscopy is also discussed.

2 Iris, slit and EM-gain calibration

The charge exchange spectroscopy system consists of a wavelength separation optical box and three spectrometers for helium, hydrogen, and carbon change exchange lines, as seen in figure 1. Thirty optical fibers with a diameter of 400 microns are inserted through port A21 (toroidal view), M21 (+45°view), and T21 (−45° view) in Wendelstein 7-X [16]. The light from the optical fiber is divided into three ranges of wavelength ($\lambda < 490$ nm, 499 nm $< \lambda <$ 546 nm, and $\lambda > 556$ nm) using 495 nm and 552 nm dichroic mirrors in the wavelength separation optical box, shown in figure 1. An iris aperture (circle or rectangle shape) is installed into each optical pass to adjust the light intensity. The helium-to-hydrogen density ratio measured with charge exchange spectroscopy is calibrated with the intensity ratio of passive emission of HeII (656.0 nm) to HI (656.3 nm) at the recombining phase. Because the light intensity of HI (656.3 nm) during the recombining phase is much larger than that during the ionizing phase, the attenuation of light intensity by the aperture iris is crucial to enabling this measurement. The width of entrance slit of each spectrometer determines the spectral resolution in the spectral measurements of charge exchange spectroscopy. The charge exchange emission contains a hot component due to the charge exchange reaction between the ion and neutral beam. It also includes a cold

2025 JINST 20 P07006

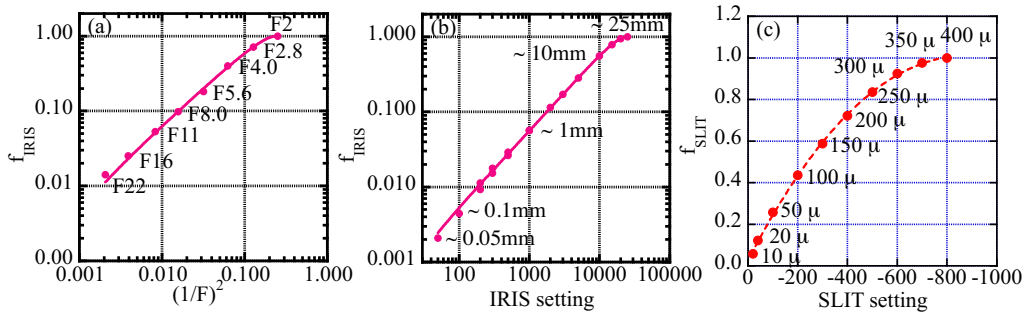

Figure 2. Aperture factor, f, by (a) circle aperture iris, (b) rectangle aperture iris of the wavelength separation optical box, and (c) slit of the spectrometer.

component due to the charge exchange reaction with a thermal neutral particle at the plasma periphery and the electron impact excitation of He^{1+} in the scrap off layer. The cold component can be subtracted by the modulation of the neutral beam by assuming no variation of thermal neutral density during the modulation. This assumption is valid for the carbon change exchange line for the measurements of core ion temperature and plasma flow velocity, but not for the helium and hydrogen charge exchange lines. There are residual cold components even after subtracting the background line emission measured at the beam-off phase. In that case, a high spectral resolution is necessary to remove the residual cold component using two Gaussian fittings. This motivates the requirement of a narrow slit width for the helium and hydrogen line measurements. Typically, the slit width is set to 50–100 μm for helium and 20 μm for the hydrogen line. The slit is fully open (400 μm) for the carbon line, where the residual cold component is negligible. The volume phase grating (VPH) with 3200/mm, 2000/mm, and 3000/mm is installed in the helium, hydrogen, and carbon spectrometers. The dispersion is 1.09 nm/mm, 1.89 nm/mm, and 1.01 nm/mm for the helium, hydrogen, and carbon spectrometers, respectively.

Figure 2 shows the aperture factor by circular aperture iris, rectangular aperture iris, and the slit normalized by the light intensity for a fully open configuration. Here, the circle aperture iris is adjustable by the F-number (the ratio of diameter to focal length) of the camera lens. The rectangle aperture iris is adjustable by the width of the aperture from 0.05 mm to 25 mm in the wavelength separation optical box. The slit width is also adjustable from 10 - 400 μm. Both rectangle aperture iris and slit width are adjustable by remote control with IRIS and SLIT settings. The iris can reduce the light intensity by more than two orders of magnitude, which is necessary for measuring the HI (656.3 nm) light intensity during the recombining phase. There is a slight leak of light even for the slit setting of zero, and the slit setting of 10 μm may have more considerable uncertainty of the calibration factor.

The Andor iXon Ultra 888 (13 × 13 μm and 1024 × 1024 pixel) is used as a detector of charge exchange spectroscopy. This detector has an electron multiplication (EM) function. When the light intensity is weak, the EM gain enables a signal to be extracted from the read-out noise. Figure 3 shows the gain factor of the EM-CCD in the helium, hydrogen, and carbon spectrometers. Here, the gain is the multiplying factor concerning the intensity of EM-gain-off, because the setting of EM-gain = 1 is not available. Although the gain factor of the EM-CCD detector in the carbon spectrometer is slightly lower than other EM-CCD at the highest gain of 300, the gain factor of the three EM-CCD detectors is almost identical. In this calibration, the EM-gain was left off because the light intensities of helium and hydrogen were large enough. However, the EM-gain can be applied in the measurements when the helium concentration is low.

2025 JINST 20 P07006

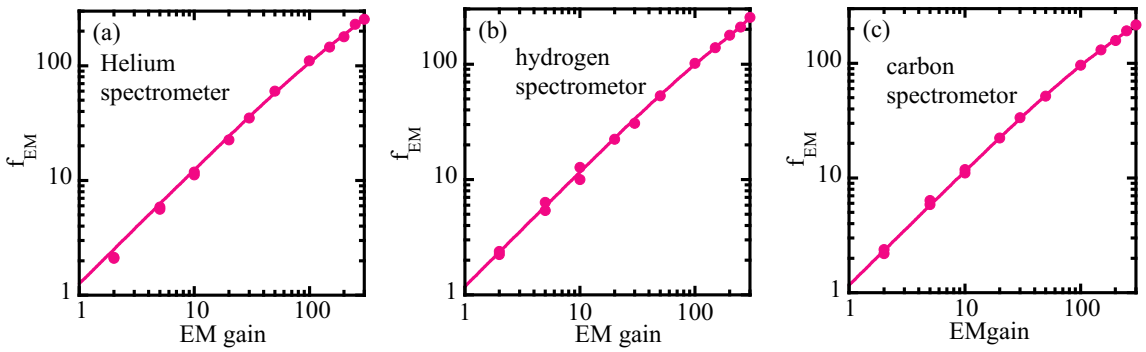

Figure 3. Gain factor, f, of electron multiplying CCD (EM-CCD) detector of helium, hydrogen, and carbon spectrometer.

3 In-situ calibration using recombining phase

The density ratio of helium to hydrogen measured with charge exchange spectroscopy is calibrated using the intensity ratio of HeII (656.0 nm) to HI (656.3 nm) in the recombining phase at the end of the discharge. It is essential that there is no neutral beam injection (NBI) during the recombining phase because the emission from the beam excitation contaminates the emission due to the recombination. Therefore, soft termination of the plasma discharge where the recombining phase appears after the NBI is desirable. The discharge where the NBI is injected, even during the recombining phase, such as radiation collapse, should be disregarded. The discharge used for this in-situ calibration is plotted in figure 4. ECH and NBI power were simultaneously switched off at 3.5 sec, and there was no radiation collapse after the heating power was switched off. The central electron temperature measured with the central ECH channel (ECE13) shows a high electron temperature of 4 keV, but it decreases to 1.5 keV as the electron density increases. The recombining phase starts when the central electron temperature drops to a few hundred eV. The central ion temperature measured with X-ray crystal spectroscopy (XICS) is comparable to the central electron temperature. The line integrated electron temperature and electron and ion temperature are almost constant during the neutral beam injection (NBI) for 1.5–3.5 sec.

After switching off the ECH and NBI power, ion and electron temperatures decay in 0.4 seconds. Then, the electron density starts to decay slightly at 3.7 sec and significantly drops from 3.8 sec to 3.85 sec due to the recombination. During this phase, all helium and hydrogen ions recombine, because the time scale of the particle transport becomes much longer than the recombining period due to the low temperature. As a result, the total intensity of the passive emission is proportional to the number of ions before the recombination. The time trace of the hydrogen fraction monitor based on the passive spectroscopic measurements of H_α (656.3 nm) and HeI (587.6 nm) intensity [19] shows that this is a helium-rich discharge. Due to the long recycling of helium, it remains relatively constant in time after the He gas flow is switched off. The active helium line HeII (468.6 nm) and hydrogen line HI (656.3 nm) due to the charge exchange recombination process between fully ionized ions and the neutral beam are measured during the NBI on (1.5 - 3.5 sec). Passive helium lines HeII (656.0 nm) and hydrogen line HI (656.3 nm) are measured during the recombining phase (3.7–3.9 sec).

Figure 5 shows the spectrum of HeII (656.0 nm) and HI (656.3 nm) at the three phases of the recombining phase measured using a hydrogen spectrometer. At the early phase of the recombining

2025 JINST 20 P07006

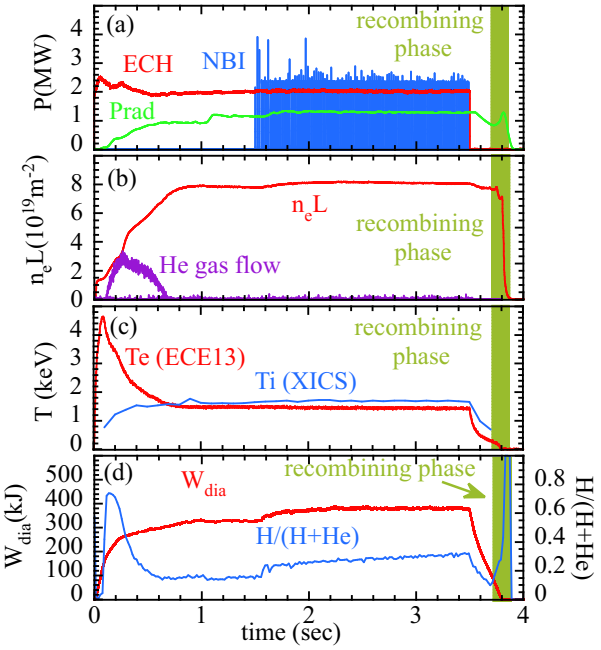

Figure 4. Time evolution of (a) heating power of ECH and NBI and radiation power, P_{rad} [17], (b) line integrated electron density, n_eL, and Helium gas flow, (c) electron temperature measured with ECE and ion temperature measured with XICS, (d) stored energy measured with diamagnetic loop [18], and the hydrogen influx monitor in discharge 20180919.027.

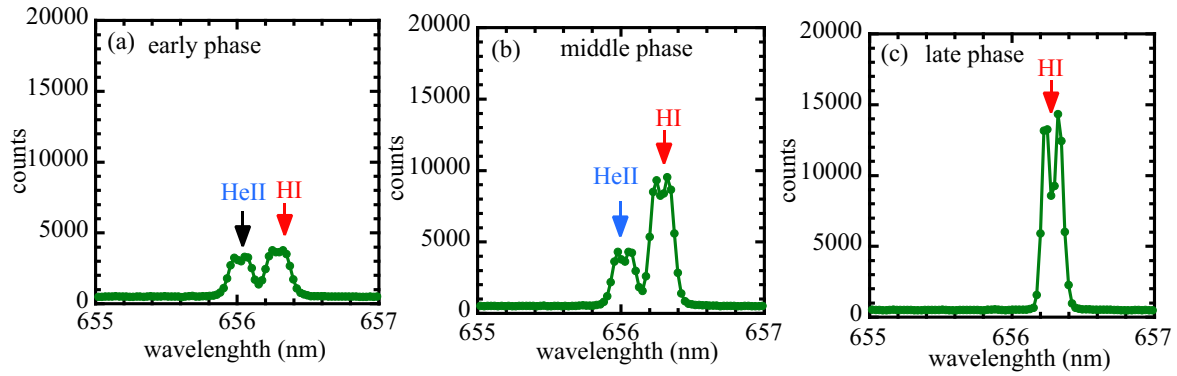

Figure 5. Spectrum of HeII (656.0 nm) and HI (656.3 nm) at (a) early (Δt = 0.26 sec), (b) middle (Δt = 0.31 sec), and (c) late (Δt = 0.32 sec) recombining phase at the central chord measured using hydrogen spectrometer with circle aperture iris of F8 and slit width of 20 µm.

process, 0.26 sec after the heating power is switched off (t = 3.76 sec), the central electron temperature drops to 0.2 keV. However, the line integrated electron density is still high at 7.7×10^{19} m^{-2}, and the HeII (656.0 nm) intensity is comparable to the HI (656.3 nm) intensity. In the middle phase, at 0.31 sec after the heating power is switched off (t = 3.81 sec), the electron temperature becomes too low to measure, and the line integrated electron density drops to 5.5×10^{19} m^{-2}. In this phase, the HI (656.3 nm) intensity increases, while the HeII (656.0 nm) intensity is similar to the level in the early phase. In the late phase at 0.32 sec, after the heating power is switched off (t = 3.82 sec), the line integrated electron density shows a further drop to 2.9×10^{19} m^{-2}. The HeII (656.0 nm) and

2025 JINST 20 P07006

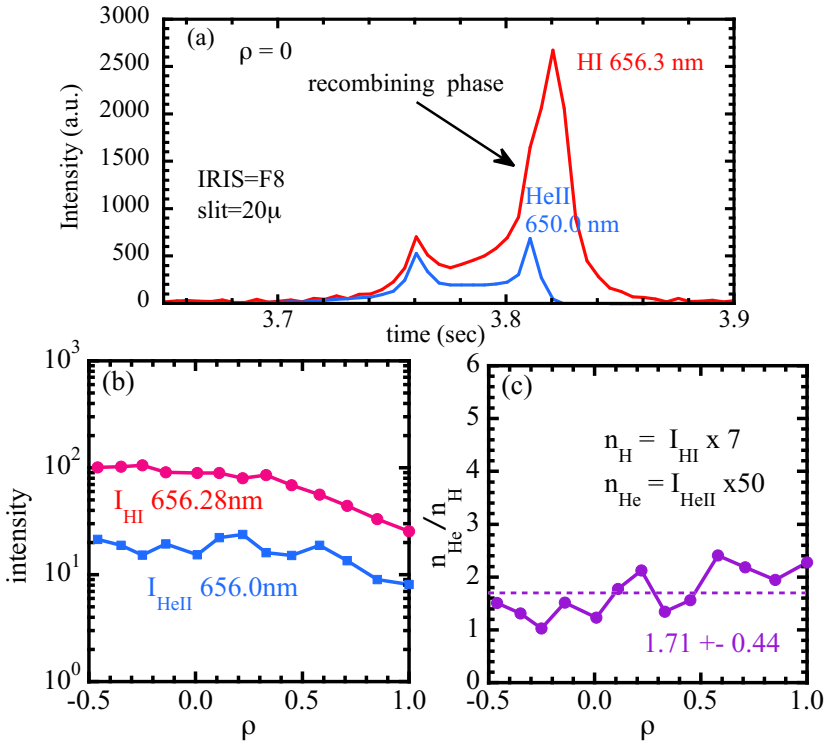

Figure 6. (a) Time evolution and of HeII (656.0 nm) and HI (656.3 nm) intensity, radial profiles of (b) time integrated HeII and HI intensity during the recombining phase, (c) density ratio of helium to hydrogen.

HeII (656.3 nm) lines almost disappear, while the HI (656.3 nm) intensity significantly increases. The decrease in the electron density is mainly due to the atomic recombining processes. The two peaks of HI (656.3 nm) are due to the Zeeman splittings.

Figure 6(a) shows the time evolution of HeII (656.0 nm) and HI (656.3 nm) intensity integrated over the spectrum in wavelength at the central chord ($\rho = 0$). Before the start of the recombining process ($t < 3.7$ sec), both HeII (656.0 nm) and HI (656.3 nm) intensities are negligibly small. Two peaks in time are observed: one at 3.76 sec and the other at 3.81 sec. The first peak appears during the temperature decay phase, while the second peak appears during the density decay phase. Although both lines increase simultaneously at the beginning of the recombining phase, the HeII (656.0 nm) line disappears earlier due to its higher ionization potential. These intensities are integrated in time during the recombining phase to evaluate the ratio of the total number of helium ions to the total number of hydrogen ions. If the radial profiles of the density ratio of helium to hydrogen are relatively flat, the absolute value of the ratio measured with change exchange spectroscopy before the recombining phase can be calibrated by the ratio of the total number of helium ions to that of hydrogen ions. Figure 6(b) shows the radial profiles of time-integrated HeII (656.0 nm) and HI (656.3 nm) intensity during the recombining phase and the density ratio of helium to hydrogen. The time-integrated HI (656.3 nm) intensity is much larger than the time-integrated HeII (656.0 nm) intensity for all chords ($\rho = -0.5$–1.0). Here, the chord for $\rho < 0$ is the high field side, and the chord for $\rho > 0$ is the low field side. The higher intensity at the high field side is due to the longer line of sight integration length. Total Helium and hydrogen densities are proportional to the integrated HeII (656.0 nm) and HI (656.3 nm) as $n_{\mathrm{He}} = \alpha\kappa_0 I_{\mathrm{HeII}}$ and $n_{\mathrm{H}} = \alpha\kappa_0 I_{\mathrm{HI}}$. Here, α includes all common optical parameters such as the line

2025 JINST 20 P07006

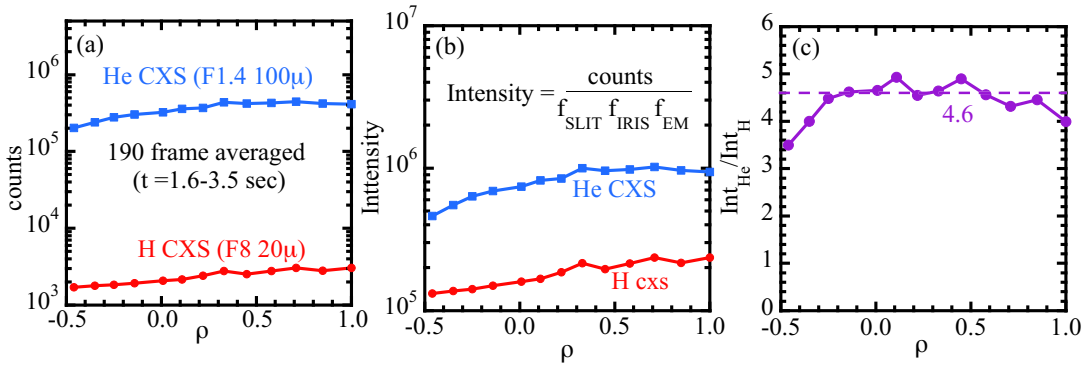

Figure 7. Radial profiles of (a) CCD counts of He and H charge exchange spectroscopy (CXS), (b) intensity corrected with slit, iris, and EM-gain facto, (c) intensity ratio of helium to hydrogen.

of sight length, optical system transmission, spectrometer sensitivity etc. According to the atomic model calculation at the recombining process, κ_0 is 50 for helium and 7 for hydrogen [20]. The radial profiles of the density ratio of helium to hydrogen using the κ_0 coefficient are plotted in figure 6(c). The ratio scatters due to the low intensity of HeII (656.0 nm) compared with HI (656.3 nm). Because the recombining region moves from the plasma periphery to the center during the recombining phase, the averaged density ratio of 1.71 ± 0.44 is taken for the calibration.

Figure 7 plots the radial profiles of helium and hydrogen intensity measured with charge exchange spectroscopy during the NBI phase. The total count of charge exchange line emission is very low due to the small aperture iris of F8 and a narrow slit width of 20 μm, which are necessary to not saturate during the recombining phase. Therefore, the 190 frames from 1.5 to 3.5 sec are averaged to improve the signal-to-noise ratio. In contrast, the He charge exchange line emission is measured with an entire open iris and a wider slit width of 100 μm, and the counts are larger than that of the hydrogen line by two orders of magnitude. Figure 7(b) shows the intensity of helium and hydrogen change exchange line emission by taking into account the slit, iris, and EM-gain factors. Figure 7(c) plots the radial profile of the intensity ratio of helium to hydrogen charge exchange line emission. The ratio is almost constant in space except for the high field side channel $\rho < 0$), where the neutral beam attenuation becomes large. The ratio taken only in the low field side ($\rho > 0$) is 4.6. Therefore, the calibration factor for the conversion from intensity ratio to density ratio is given by using the density ratio at the recombining phase, and the density ratio can be given as $n_{\mathrm{He}}/n_{\mathrm{H}} = 0.37$ ($Int_{\mathrm{He}}/Int_{\mathrm{H}}$). The systematic error due to the uncertainty of density ratio measurements during the recombining phase is about 30% at largest [20].

4 Comparison of central density ratio of helium to hydrogen to the influx ratio

The central density ratio of helium to hydrogen is evaluated using the calibration factor obtained from the calibration described above. Figure 8 shows the time evolution of the central density ratio of helium to hydrogen and the influx ratio evaluated from the H/(H+He) monitor for high and low Helium concentration discharges. The central density ratio of helium to hydrogen is around unity ($n_{\mathrm{He}} \sim n_{\mathrm{H}}$) and is almost constant in time in the helium-rich discharge (figure 8(a)). However, the influx ratio increases as the ECH power is stepped down from 4 MW to 1.2 MW (4 MW for t = 0.3–4.0 sec, 2.4 MW for t = 4.0–5.5 sec, 1.8 MW for t = 5.5–7.0 sec, 1.2 MW for t = 7.0–8.5 sec). This implies that

2025 JINST 20 P07006

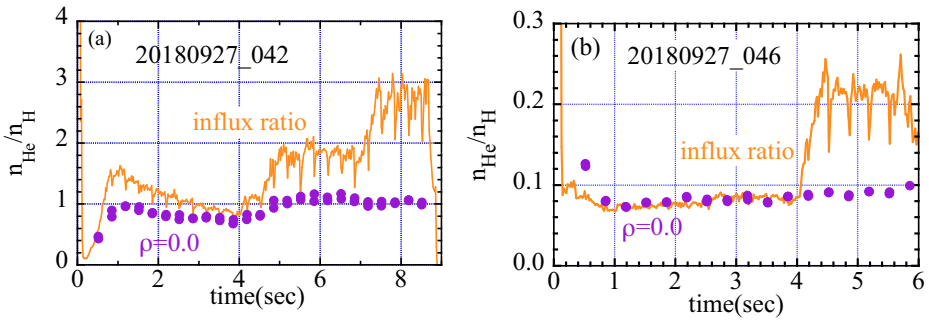

Figure 8. Time evolution of central density ratio derived from the calibrated charge exchange spectroscopy and influx ratio of helium to hydrogen from passive spectroscopy in the discharge with (a) high and (b) low helium concentration.

the helium concentration in the plasma core increases as the ECH power decreases. Instead, the charge exchange spectroscopy disagrees with this conclusion. Similar behavior is observed in the discharge with low helium concentration (figure 8(b)). The central density ratio of helium to hydrogen is around 10% ($n_{He} \sim n_H/10$) and is almost constant in time. However, the influx ratio increases as the ECH power is stepped down from 4 MW to 1.2 MW (4 MW for t = 0.3–2.5 sec, 3.4 MW for t = 2.5–4.0 sec, 1.8 MW for t = 4.0–5.5 sec, 1.2 MW for t = 5.5–6.2 sec). The increase in the influx ratio of helium to hydrogen is mainly due to the drop of H_α (656.3 nm) intensity, not the change in HeI (587.6 nm) intensity. This example indicates that the central density ratio of helium to hydrogen is consistent with the influx ratio for the discharge with higher ECH power but not with lower ECH power. The influx ratio is calculated from the intensity ratio of HeI (587.6 nm) emission to H_α (656.3 nm) emission. Plasma parameters such as density and temperature in the emission region are necessary as input parameters to calculate the influx ratio from the intensity ratio with the collisional-radiative model. Due to a lack of precise measurements of plasma parameters in the emission region, assumptions for the plasma temperature and density are made. The influx ratio measurement relies heavily on assumptions about the edge conditions since it is based on SXB coefficients and line integrals at some arbitrary position in the scrape-off layer. It is near, but not quite on the intersection of the outermost flux surface of the edge magnetic islands with the divertor target plates (strike lines). As the ECRH power changes, the scrape off layer conditions can change significantly, moving the emission and ionization regions around. The core measurement is not sensitive to any of these assumptions. Therefore, the estimation of the influx ratio is sensitive to the edge plasma condition, while that of charge exchange spectroscopy does not depend on the edge plasma condition.

Another comparison was made for the discharge with hydrogen pellet injections [21], as seen in figure 9. The hydrogen pellet is injected into the plasma at t = 4.6, 4.84, and 4.94 sec, as seen in the time evolution of line-integrated electron density. Before the pellet injection, the central density ratio of helium to hydrogen is consistent with the influx ratio, However, the discrepancy between charge exchange spectroscopy and influx monitor is observed after the pellet injections. Charge exchange spectroscopy clearly observes the drops in the central density ratio of helium to hydrogen due to the hydrogen pellet injection. The ratio drops from 1.0 to 0.83 and to 0.71 after the first and second pellets, respectively. These drops are roughly consistent with the increase of line integrated electron density of 10% measured with a laser interferometer. The influx ratio shows a large spike only at t = 4.6 sec but does not show the step-down behavior caused by multiple pellet injections. This is because the pellet hydrogen has not left the plasma and recycled yet.

2025 JINST 20 P07006

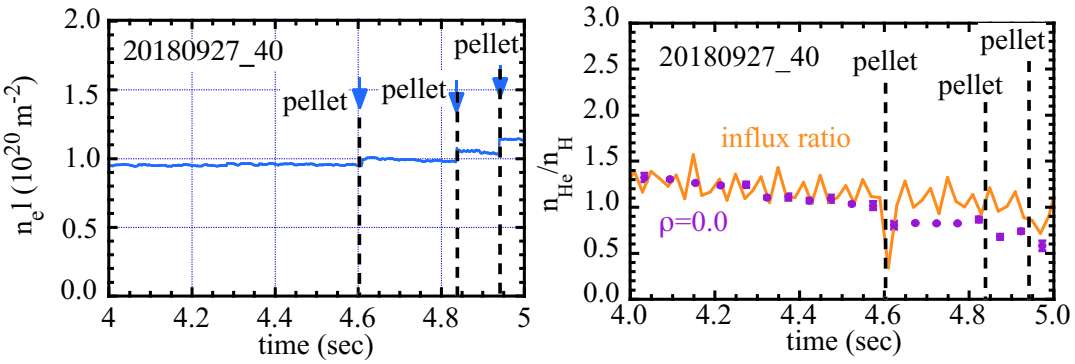

Figure 9. Time evolution of (a) line integrated electron density and (b) central density derived from the calibrated charge exchange spectroscopy and influx ratio of helium to hydrogen from passive spectroscopy in the discharge with hydrogen pellet injections. The error bars plotted in figure 9(b) are the relative uncertainty of the ratio, not the absolute uncertainty which is roughly 25%.

5 Summary

The charge exchange spectrometers for spatially resolved measurements of helium-hydrogen density ratio are calibrated by the density ratio of helium to hydrogen estimated from the line ratio of HeII (656.0 nm) to HI (656.3 nm) observed in the recombining phase after the heating power is switched off. This is an in-situ calibration using the helium and hydrogen mixture plasma, which differs from the conventional calibration based on the absolute intensity calibration of the charge exchange spectroscopy system and emission cross-section with considerable uncertainty. The density ratio of helium to hydrogen measured with charge exchange spectrometers calibrated with this method is compared with the influx ratio evaluated from the passive spectroscopy. These two ratios agree in the discharge with higher ECH power but not with lower ECH power. Since the measurements using charge exchange spectroscopy indicate that the ratio of helium to hydrogen does not depend much on ECH power, the large increase in the influx ratio evaluated from the passive spectroscopy would be attributed to the change in plasma parameters near the divertor, such as electron temperature. The core density ratio of helium to hydrogen measured with this charge exchange spectrometer drops at the timing of hydrogen pellet injections, while the influx ratio evaluated from passive spectroscopy does not show these drops. The drop in the ratio observed in charge exchange spectroscopy is quantitatively consistent with the jump of electron density measured with a laser interferometer. The core density ratio of helium to hydrogen evaluated by these charge exchange spectrometers will provide essential information to optimize the helium concentration in the helium-hydrogen mixture plasma's ion cyclotron resonance heating (ICRH).

Acknowledgments

The authors wish to thank the Wendelstein 7-X Experiment Group for the excellent support of this work. This work is supported by the JSPS KAKENHI Grant Numbers JP21H04973. This work has been carried out within the framework of the EUROfusion Consortium, funded by the European Union via the Euratom Research and Training Programme (Grant Agreement No. 101052200-EUROfusion). Views and opinions expressed are, however, those of the authors only and do not necessarily reflect those of the European Union or the European Commission. Neither the European Union nor the European Commission can be held responsible for them.

2025 JINST 20 P07006

References

[1] R.J. Fonck et al., *Spatially Resolved Measurements of Fully Ionized Low-Z Impurities in the PDX Tokamak*, *Phys. Rev. Lett.* **49** (1982) 737.

[2] M.G. von Hellermann et al., *Visible charge exchange spectroscopy at JET*, *Rev. Sci. Instrum.* **61** (1990) 3479.

[3] M. Yoshinuma et al., *LETTER: Observation of an impurity hole in the Large Helical Device*, *Nucl. Fusion* **49** (2009) 062002.

[4] K. Ida et al., *Observation of an impurity hole in a plasma with an ion internal transport barrier in the Large Helical Device*, *Phys. Plasmas* **16** (2009) 056111.

[5] R.M. McDermott et al., *Evaluation of impurity densities from charge exchange recombination spectroscopy measurements at ASDEX Upgrade*, *Plasma Phys. Control. Fusion* **60** (2018) 095007.

[6] R.J. Fonck and R.A. Hulse, *He^{++} Transport in the PDX Tokamak*, *Phys. Rev. Lett.* **52** (1984) 530.

[7] K. Ida et al., *Measurement of radial profiles of density ratio of helium to hydrogen ion using charge exchange spectroscopy with two-wavelength spectrometer*, *Rev. Sci. Instrum.* **86** (2015) 123514.

[8] K. Ida et al., *Helium transport in the core and stochastic edge layer in LHD*, *Plasma Phys. Control. Fusion* **58** (2016) 074010.

[9] K. Ida et al., *Measurements of radial profile of hydrogen and deuterium density in isotope mixture plasmas using bulk charge exchange spectroscopy*, *Rev. Sci. Instrum.* **90** (2019) 093503.

[10] S.R. Haskey et al., *Radially resolved active charge exchange measurements of the hydrogenic isotope fraction on DIII-D*, *Rev. Sci. Instrum.* **92** (2021) 043535.

[11] M. Yoshinuma et al., *Measurements of radial profile of isotope density ratio using bulk charge exchange spectroscopy*, *Rev. Sci. Instrum.* **92** (2021) 063509.

[12] K. Ida and T. Kato, *Line-emission cross sections for the charge-exchange reaction between fully stripped carbon and atomic hydrogen in tokamak plasma*, *Phys. Lett. A* **166** (1992) 35.

[13] W.M. Solomon et al., *Experimental test of the neoclassical theory of impurity poloidal rotation in tokamaks*, *Phys. Plasmas* **13** (2006) 056116.

[14] J. Chen et al., *Effect of energy dependent cross-section on flow velocity measurements with charge exchange spectroscopy in magnetized plasma*, *Phys. Lett. A* **383** (2019) 1293.

[15] K. Ida et al., *Verification of Carbon Density Profile Measurements with Charge Exchange Spectroscopy Using Hydrogen and Deuterium Neutral Beams*, *Plasma Fusion Res.* **14** (2019) 1402079.

[16] O.P. Ford et al., *Visible core spectroscopy at Wendelstein 7-X*, *Rev. Sci. Instrum.* **95** (2024) 083526.

[17] D. Zhang et al., *Bolometer tomography on Wendelstein 7-X for study of radiation asymmetry*, *Nucl. Fusion* **61** (2021) 116043.

[18] K. Rahbarnia et al., *Diamagnetic energy measurement during the first operational phase at the Wendelstein 7-X stellarator*, *Nucl. Fusion* **58** (2018) 096010.

[19] Y. Wei et al., *Spectroscopic studies of fuel recycling and impurity behaviors in the divertor region of Wendelstein 7-X*, *Plasma Sci. Technol.* **21** (2019) 105102.

[20] M. Goto et al., *Determination of the hydrogen and helium ion densities in the initial and final stages of a plasma in the Large Helical Device by optical spectroscopy*, *Phys. Plasmas* **10** (2003) 1402.

[21] J. Baldzuhn et al., *Pellet fueling experiments in Wendelstein 7-X*, *Plasma Phys. Control. Fusion* **61** (2019) 095012.

2025 JINST 20 P07006